Journal of
Marine Science and Engineering

Article

Abatement of Ocean-Wave Impact by Crevasses in an Ice Shelf

Yuri V. Konovalov

Mathematical Department, Financial University under the Government of the Russian Federation, Leningradsky Prospekt 49, 125993 Moscow, Russia; yvkonovalov@fa.ru

Abstract: Forced ice-shelf oscillations modeling was undertaken employing a full 3D finite-difference model of an elastic ice shelf that was coupled to a treatment of under-shelf seawater flux. The seawater flux was described by the wave equation, which includes the pressure excitements in the shallow water layer under the ice shelf. Thus, ice-shelf flexure was produced by hydrostatic pressure oscillations in the below-shelf seawater. Numerical calculations were performed for an idealized rectangular crevasse-ridden ice-shelf geometry. The crevasses were modeled as rectangular notches into the ice shelf. In the numerical experiments, the ice-plate flexures were forced by harmonic-entering pressure oscillations having a range of periodicities 5–250 s. The dispersion spectra derived for a crevasse-ridden ice shelf revealed "band gaps"—frequency ranges where no eigenmodes exist. The results further showed that the impact of ocean waves on the ice plate is abated from the point of view of a decrease in the spectral average amplitude in the vicinity of the spectrum where the "band gaps" are observed. This impact depends on the depth of crevasse penetration to the ice.

Keywords: ice shelf modeling; ice shelf vibration; crevasse-ridden ice shelf; dispersion spectrum; inter-mode spaces

check for updates

Citation: Konovalov, Y.V. Abatement of Ocean-Wave Impact by Crevasses in an Ice Shelf. *J. Mar. Sci. Eng.* **2021**, *9*, 46. https://doi.org/10.3390/jmse9010046

Received: 9 December 2020
Accepted: 29 December 2020
Published: 4 January 2021

1. Introduction

Tides and ocean swell causing hydrostatic pressure excitements in the under-shelf seawater layer generate ice-shelf flexure, and thus can launch the processes that lead to destruction of ice in those ice shelves and maintain ice-shelf rift propagation [1–6]. The effect of tides and ocean swell is an essential part of the overall impact [7] that produces ice calving in ice shelves [8,9].

In particular, the observations on the Ross Ice Shelf reveal that the gravity waves cause vibrations in ice shelves [6,10–14]. The investigations showed that the response of the Ross Ice Shelf depends on the frequency and amplitude of the gravity-wave forcing and that the response varies with seasons, so the ice temperature affects the mechanical properties of the ice and, therefore, signal propagation characteristics [10]. The response of the ice shelf (Ross Ice Shelf) to the gravity waves and to the swell impacts is more significant than that observed at the Scott Base and in the Dry Valleys [10]. The observations in 2014 undertaken on the Ross Ice Shelf revealed that the signals propagate as Rayleigh–Lamb waves in the ice-shelf/seawater cavity system that are generated by ocean-wave interactions nearer the shelf front [11]. The infragravity waves' impact and the Chilean earthquake tsunami response were observed on the Ross Ice Shelf (for one year from November 2014) as ice-shelf/seawater-coupled flexural waves [12]. The observations from November 2014 to November 2016 on the Ross Ice Shelf also revealed the propagation of the flexural-gravity waves and extensional Lamb waves in the ice-shelf/seawater cavity system [13]. The strongest icequakes were observed at the ice front during the austral summer when swell impacts are significant due to minimal sea ice [14].

Moreover, the resonant-like vibration that can appear under long-term swell forcing at near-eigen frequencies (the impact over many swell periods) can cause fracture in the ice shelf (e.g., [1,15]). Thus, knowledge of the process of vibration in ice shelves is significant for comprehending ice-sheet–ocean interactions and ice-shelf stability. In this respect, scientific interest in the problem of vibration in ice shelves motivates the development of flexure and vibration models (e.g., [1–3,16–32]), based on elastic thin-plate/elastic beam approximations that can be considered as the result of the vertical integration of the full 3D momentum equations [25,26]. These models allow deriving ice-shelf deformations and simulating the bending stresses. There are models among these that consider coupled ice-shelf/sub-ice-shelf cavity systems [1,25–32] and permit estimating possible effects of tides and ocean-swell actions on the calving process. In particular, these models allow consideration of the eigenvalue problem for the ice-shelf/sub-ice seawater systems [1,28] that has interest from the point of view of possible resonances in the system.

Further advancement of elastic-beam models occurred in the direction of visco-elastic rheological model development. In particular, tidal flexure of an ice shelf was obtained using the linear visco-elastic Burgers model [33,34], the nonlinear thin-plate visco-elastic model [35], and the nonlinear 3D visco-elastic full-Stokes model [36].

In particular, this previous modeling provides a way to conduct spectral analysis of the problem of ice shelves and ocean-waves interaction, and to provide a description of the eigen-frequencies and eigenmodes of the ice-shelf vibration (e.g., [1]). Furthermore, investigation of the dispersion spectra reveals that the spectra obtained for an ice shelf with crevasses can be qualitatively different from when crevasses are missing [37]. Crevasses are widely distributed features in all ice shelves, and their appearance, growth, and penetration are the subject of many studies (e.g., [38–40]). Essentially, the dispersion spectra obtained for a crevasse-ridden ice shelf reveal the "band gaps" that are absent from the spectra obtained for an ice shelf without crevasses. These "band gaps" are the frequency ranges over which no eigenmodes exist [37] with a phenomenon that emerges when a wave is propagated through a periodic structure [41] and which we meet in many different applications, including crystallography; phononic crystals; electron transport in metals and semiconductors [42]; the formation of nearshore, underwater sandbars [43]; and gravity-wave propagation through periodical structures of floating ice [44–48].

In [37], the propagation of high-frequency elastic-flexural waves through a floating ice shelf was investigated by a 2D model, and the numerical calculations were performed by COMSOL (finite-elements method). The band gap was observed from 0.2 to 0.38 Hz for a crevasse-ridden ice shelf that was 50 km length and 300 m thick with crevasses spaced 500 m apart [37].

In this study, a model of forced vibrations of an ice plate, floating in shallow water, was developed using a full 3D finite-difference treatment of elastic flexure that also takes into account under-shelf seawater flow. In this model the ice-shelf flexure is described by the 3D momentum equations for an elastic substance (e.g., [49,50]) thereby eliminating the need for assumptions associated with typical thin-plate treatments in the past. The under-shelf seawater flow, which essentially is the under-shelf seawater swell in the problem of ice-shelf and ocean-swell interaction, is described by the 2D wave equation [1].

In this study, the numerical experiments were undertaken both for an uninjured ice shelf free of crevasses and for a crevasse-ridden ice shelf, both of which have an idealized rectangular geometry (the aspect ratio is about the same as in [37]. The crevasses were considered as rectangular notches into the ice shelf (e.g., [37]). The obtained dispersion spectra reveal intermode spaces (regular spaces between two modes) that make the nth mode transitions. The intermode spaces of modes for ice shelves that lack crevasses constitute a regular pattern, whereas the intermode spaces of modes for ice shelves that have crevasses are regular over distinct frequency regions and are completely absent over "band gap" regions. The intermode spaces coincide with the minima in the amplitude spectrum. Moreover, the dispersion spectra derived for a crevasse-ridden ice shelf reveal the "band gaps"—the frequency ranges where no eigenmodes exist [37]. This study is focused on the investigation of how the width of "band gaps" increases as the result of the growth in the crevasses' penetration depth.

2. Field Equations

The momentum equations that describe ice-shelf flexure, based on Hooke's law, are expressed as (e.g., [49])

$$\begin{cases} \frac{2(1-\nu)}{1-2\nu}\frac{\partial^2 U}{\partial x^2}+\frac{\partial^2 U}{\partial y^2}+\frac{\partial^2 U}{\partial z^2}+\frac{1}{1-2\nu}\left(\frac{\partial^2 V}{\partial x\,\partial y}+\frac{\partial^2 W}{\partial x\,dz}\right)=\frac{2(1+\nu)}{E}\rho\,\frac{\partial^2 U}{\partial t^2}; \\ \frac{\partial^2 V}{\partial x^2}+\frac{2(1-\nu)}{1-2\nu}\frac{\partial^2 V}{\partial y^2}+\frac{\partial^2 V}{\partial z^2}+\frac{1}{1-2\nu}\left(\frac{\partial^2 U}{\partial y\,\partial x}+\frac{\partial^2 W}{\partial y\,\partial z}\right)=\frac{2(1+\nu)}{E}\rho\,\frac{\partial^2 V}{\partial t^2}; \\ \frac{\partial^2 W}{\partial x^2}+\frac{\partial^2 W}{\partial y^2}+\frac{2(1-\nu)}{1-2\nu}\frac{\partial^2 W}{\partial z^2}+\frac{1}{1-2\nu}\left(\frac{\partial^2 U}{\partial z\,\partial x}+\frac{\partial^2 V}{\partial z\,\partial y}\right)-\frac{2(1+\nu)}{E}\rho g=\frac{2(1+\nu)}{E}\rho\,\frac{\partial^2 W}{\partial t^2}; \\ 0<x<L; y_1(x)<y<y_2(x);\ h_b(x,y)<z<h_s(x,y); \end{cases} \quad (1)$$

where (XYZ) is a rectangular coordinate system with the X axis along the central line, and the Z axis pointing vertically upward; U, V and W are the two horizontal and one vertical ice displacements, respectively; and ρ is ice density. The geometry of the ice shelf is assumed to be given by lateral boundary functions $y_{1,2}(x)$ at sides labeled 1 and 2 and functions for the surface and base elevations, $h_{s,b}(x,y)$, denoted by subscripts s and b, respectively.

The sub-ice water flow is described by the wave equation [1]:

$$\frac{\partial^2 W_b}{\partial\, t^2}=\frac{1}{\rho_w}\frac{\partial}{\partial\, x}\left(d_0\frac{\partial\, P'}{\partial\, x}\right)+\frac{1}{\rho_w}\frac{\partial}{\partial\, y}\left(d_0\frac{\partial\, P'}{\partial\, y}\right), \quad (2)$$

where ρ_w is seawater density; $d_0(x,y)$ is the depth of the sub-ice water layer; $W_b(x,y,t)$ is the vertical deflection of the ice-shelf base and $W_b(x,y,t)=W(x,y,h_b(x,y),t)$; and $P'(x,y,t)$ is the deviation of the sub-ice water pressure from the hydrostatic value.

The boundary conditions to the ice shelf are: (i) a stress-free ice surface; (ii) the normal stress exerted by seawater at the ice-shelf free edges and at the ice-shelf base; and (iii) rigidly fixed edges at the grounding line of the ice shelf.

In [51], the linear combination of the boundary conditions was considered. In this study, the parameters of this combination were taken as $\alpha_1=1$ and $\alpha_2=0$ (see Equation (3) in [51,52]).

The boundary conditions to the seawater layer correspond to the frontal incident wave. They are

$$\text{(i)}\ \rightarrow\ \text{at } x=0:\ \frac{\partial P'}{\partial x}=0;$$
$$\text{(ii)}\ \rightarrow\ \text{at } y=y_1,\ y=y_2\text{:}\ \frac{\partial P'}{\partial y}=0;$$

at $x=L$: $P'=A_0\,\rho_w g\,e^{i\omega t}$, where A_0 is the amplitude of the incident wave.

The detailed description of the problem set-up is provided in [52].

3. Numerical Experiments

The numerical experiments with forced vibrations were undertaken for a physically idealized ice shelf with the geometry of a rectangular parallelepiped. In the undeformed ice shelf, the four edges had coordinates $x=0$, $x=L$, $y_1=0$, $y_2=B$, where L is the plate length along the X axis and B is the plate width along the Y axis ($B=y_2-y_1$, see Equation (1)).

The ice plate had only one fixed edge (at $x=0$), while the other edges (at $x=L$, $y_1=0$, $y_2=B$) were free. This is the special case of an ice shelf that is also known as an "ice tongue" (e.g., [1]). The intact ice tongue without crevasses was 16 km in longitudinal extent, 0.8 km width and 100 m thick. The water-layer depth in the case of the intact ice tongue was a constant value of 100 m.

The crevasses were considered as rectangular notches into the ice tongue [37]. The crevasses were located across the ice tongue periodically along the *X* axis with the spacing denoted by Δl_{cr}. The width of the crevasses is denoted by w_{cr} and the penetration depth of the crevasses is denoted by d_{cr}. Figure 1 shows the cross-section along the centerline of the crevasse-ridden ice tongue considered in this study.

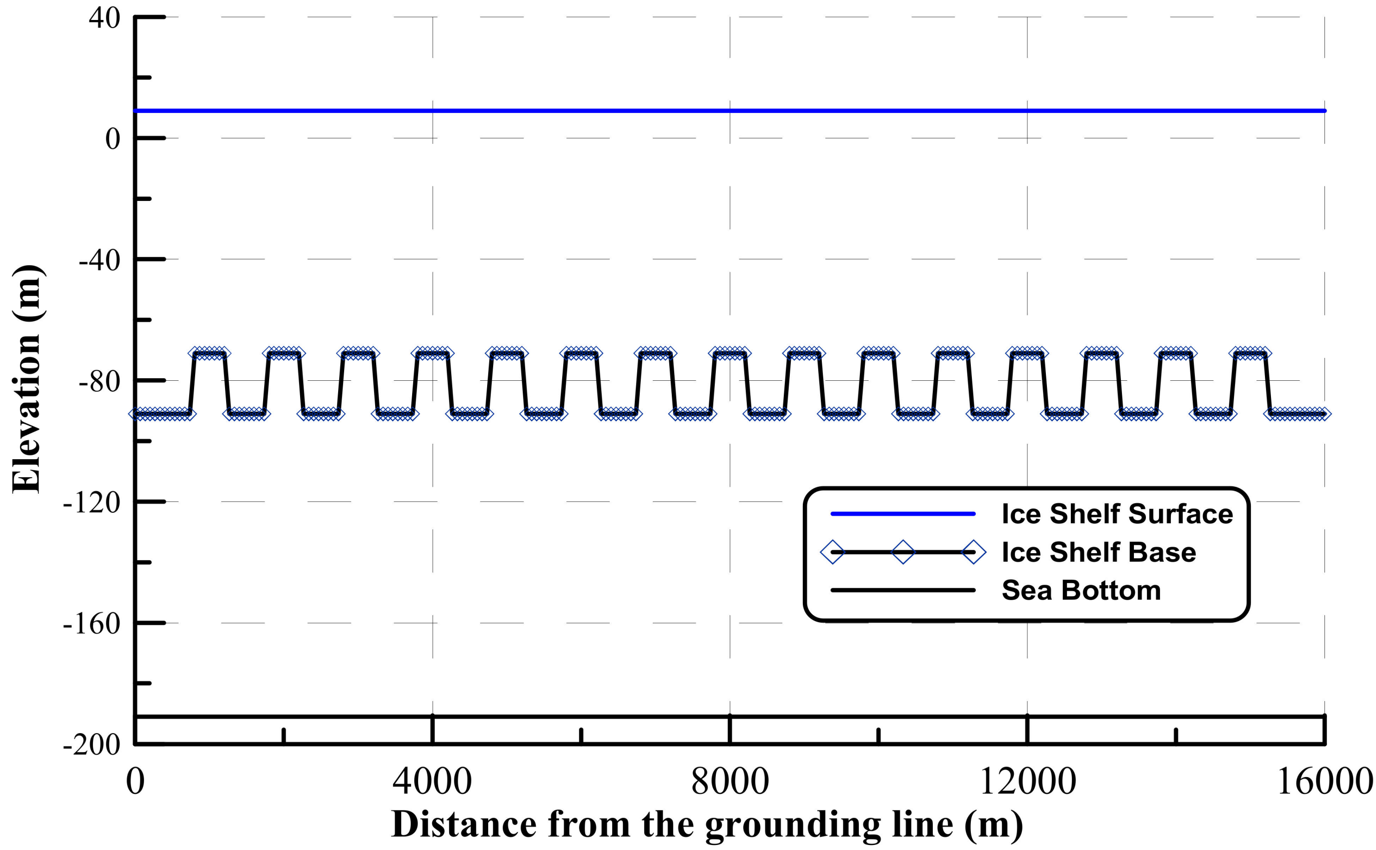

Figure 1. The crevasse-ridden ice-shelf geometry and the cavity geometry that are considered in the numerical experiments. Spatial periodicity (Δl_{cr}) of the crevasses is equal to 1 km. The width of the crevasses (w_{cr}) is equal to 500 m, and the penetration depth (d_{cr}) of the crevasses is equal to 20 m.

The numerical experiments with the crevasse-ridden ice tongue were performed for a range of the periodicities of the incident wave from 5 s to 250 s. In this range there are two “band gaps” that can be distinguished in the dispersion spectra for the given parameters of the crevasse-ridden ice tongue. Figures 2 and 3 show the parts of the spectra in which the two “band gaps” are observed.

Figure 4 shows the relation between the width of the “band gap” derived from the model and the depth of the crevasses’ penetration to the ice tongue.

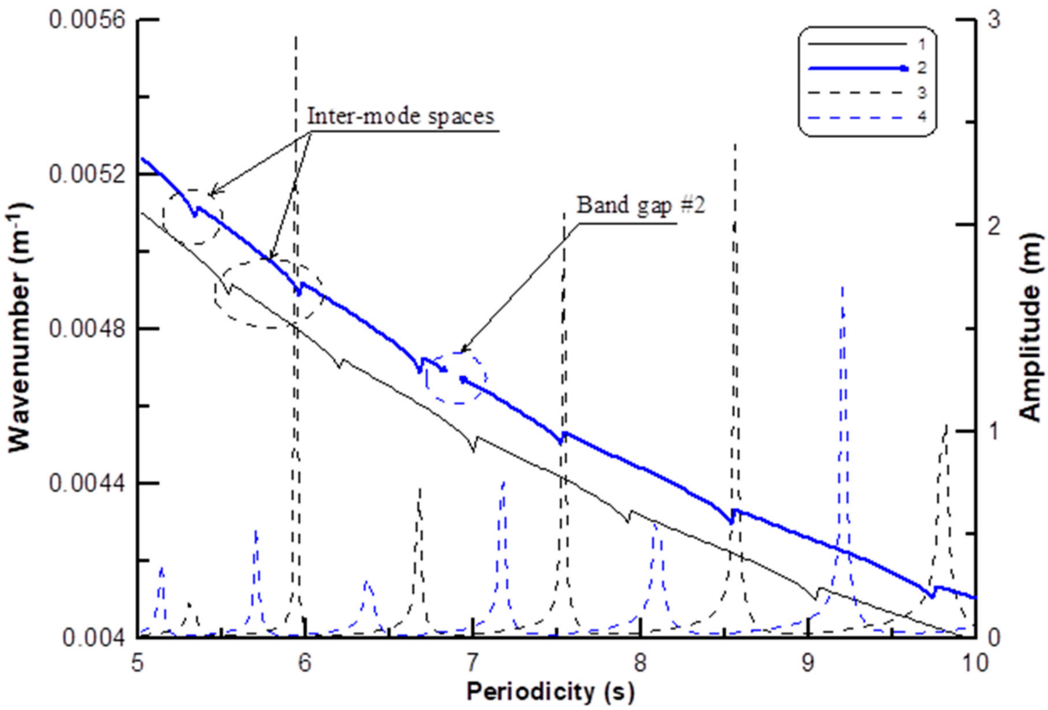

Figure 2. The dispersion spectra (curves 1–2) and the amplitude spectra (curves 3–4). The ice-shelf length is 16 km, the width is 0.8 km, and the thickness is 100 m. 1—the dispersion spectrum obtained for the intact ice shelf free of crevasses. 2—the dispersion spectra obtained for the crevasse-ridden ice shelf ($d_{cr} = 20$ m). Curves 3 and 4 are the amplitude spectra obtained, respectively, for the intact ice shelf free of crevasses and for the crevasse-ridden ice shelf ($d_{cr} = 20$ m). Spatial periodicity of the crevasses is equal to 1 km. Young's modulus = 9 GPa, Poisson's ratio $\nu = 0.33$ [53].

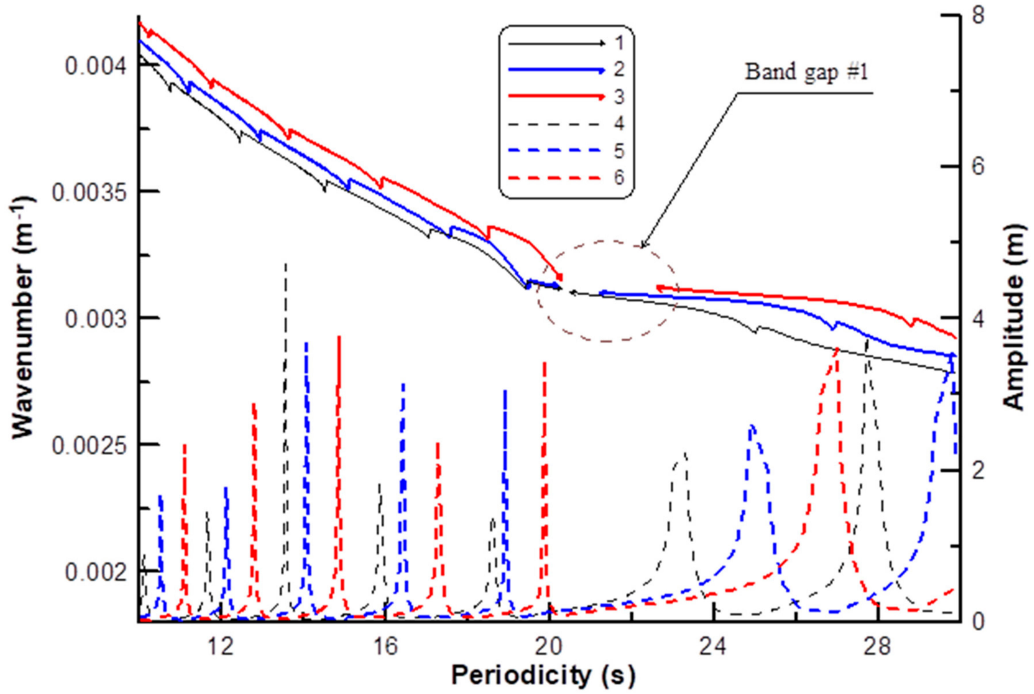

Figure 3. The dispersion spectra (curves 1–3) and the amplitude spectra (curves 4–6). The ice shelf length is 16 km, the width is 0.8 km, and the thickness is 100 m. Curves 1—3 are the dispersion spectra obtained for the crevasse-ridden ice shelf: 1—$d_{cr} = 10$ m; 2—$d_{cr} = 20$ m; 3—$d_{cr} = 30$ m. Curves 4–6 are the amplitude spectra obtained for the crevasse-ridden ice shelf: 4—$d_{cr} = 10$ m; 5—$d_{cr} = 20$ m; 6—$d_{cr} = 30$ m where d_{cr} is the crevasses depth. Spatial periodicity of the crevasses is equal to 1 km. Young's modulus = 9 GPa, Poisson's ratio $\nu = 0.33$ [53].

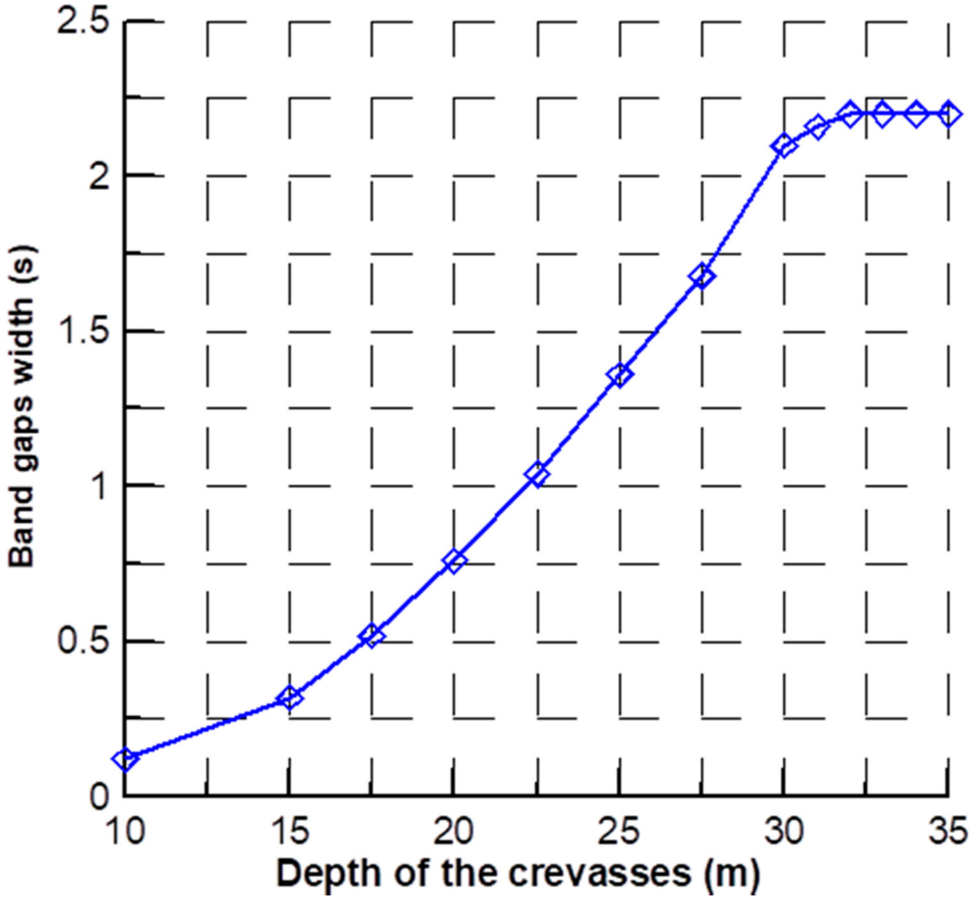

Figure 4. Band-gap width (the "band gap" is shown in (Figure 3)) versus depth of the crevasse.

4. Discussion

The obtained dispersion spectra are not continuous (Figures 2 and 3). The spectra reveal intermode spaces that are observed both for the uninjured ice tongue free of crevasses and for the crevasse-ridden ice tongue. These intermode spaces provide the transition from n-th mode to (n + 1)-th mode. They coincide with the minima in the amplitude spectrum (Figures 2 and 3). That is, the ice tongue substantially reduces the incident wave at this transition.

Moreover, the dispersion spectra reveal the "band gaps" that are the ranges of periodicities where the modes of the ice tongue vibrations change rapidly (curves 2, 3 in Figure 5), in opposite to the ranges outside the "band gaps", where the modes change continuously (curves 1 and 4 in Figure 5). In the considered range of the forcing (incident wave) periodicity 5–250 s, which includes ocean swell and infragravity waves [6], there exist two "band gaps": at about 6–7 s (Figure 2) and at about 20–24 s (Figure 3). In Figure 2, the "band gap" corresponds to the second Bragg wave (e.g., [45,54]), and the modeled wavelength is about 1.3 km. In Figure 3, the "band gap" corresponds to the first Bragg wave, and the modeled wavelength is about 2 km.

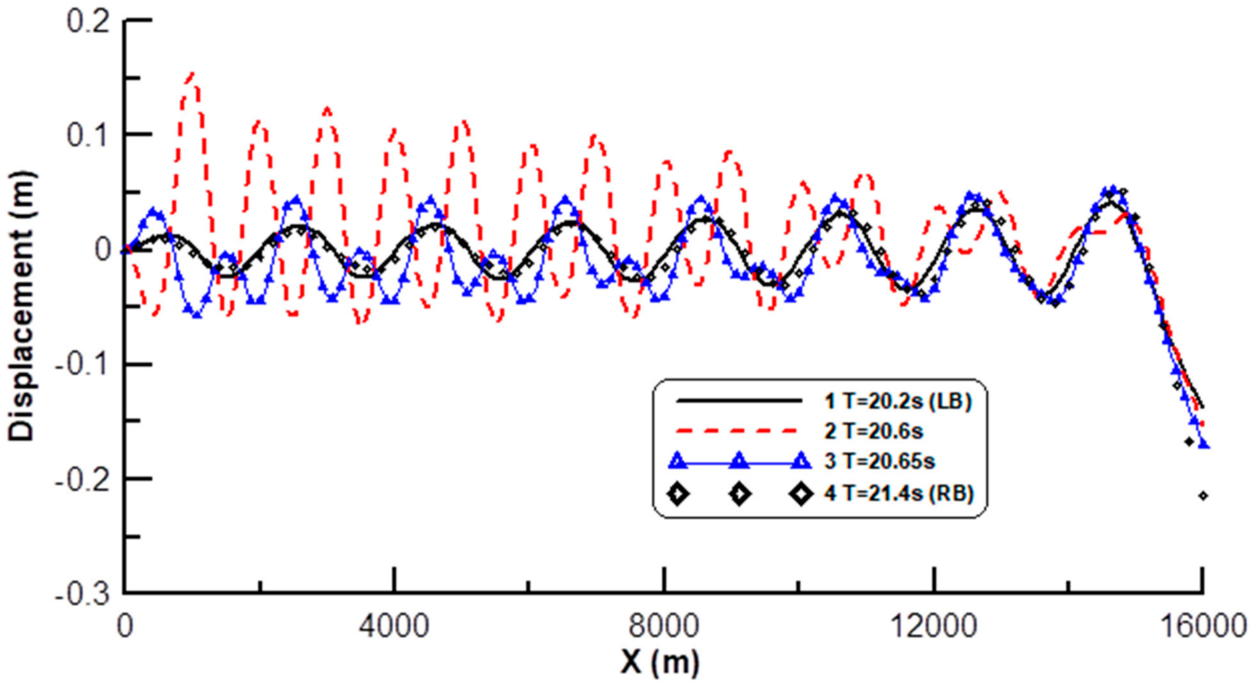

Figure 5. Ice-tongue flexures along the central line obtained at different periodicities of the forcing (T) beside and inside the first "band gap" (Figure 3). Curves 1 and 4 are the ice-tongue flexures beside the first "band gap", respectively, obtained at T = 20.2 s and at T = 21.4 s. Curves 2 and 3 are the ice-tongue flexures inside the first "band gap", respectively, obtained at T = 20.6 s and at T = 20.65 s. The crevasses' depth is equal to 20 m. Spatial periodicity of the crevasses is equal to 1 km.

The overall width of the "band gaps" increases with growth in the crevasse depth (the effect especially appears for the first "band gap" (Figure 3)) until the crevasses' depth achieves the value at which the "band gaps" width reaches the maximum value (Figure 4). For the first "band gap" (Figure 3), the maximum level of the "band gap" width is about 2.2 s, and this maximum is reached at a crevasse depth of about 30 m (Figure 4).

Essentially, from Figure 3, we can establish that the increase yields the decrease in the spectral average (in the given range of periodicities) amplitude of the ice-tongue vibrations. Indeed, in Figure 3 we see that the number of the resonant peaks decreases (in the given range 10–30 s) when the band-gap width increases. Therefore, the integral $\int_{T_1}^{T_2} A(T)dT$ should decrease (and this decrease means the spectral average amplitude will also decrease) as the band-gap width rises.

In particular, the values of the spectral average amplitude obtained for the spectral range in Figure 3 are, respectively, equal to 0.6438 m for curve 4 ($d_{cr} = 10$ m) and to 0.5307 m for curve 6 ($d_{cr} = 30$ m) (all in Figure 3).

Moreover, the similar trend can be observed in the exact solutions obtained for some simpler systems as, for instance, the shallow water channel with the free water surface.

The long gravity waves in the shallow water channel are described by the wave equation (e.g., [55,56]):

$$\frac{\partial^2 W}{\partial t^2} = g d_0 \left(\frac{\partial^2 W}{\partial x^2} + \frac{\partial^2 W}{\partial y^2} \right); \; 0 < x < L; \; y_1(x) < y < y_2(x); \tag{3}$$

where $W(x, y, t)$ is the free surface elevation from the nonperturbed water surface in the channel.

Considering one-dimensional free harmonic vibrations of the gravity wave, which propagate along the X axis in the channel with the crevasse-ridden bottom (Figure 6), after the separation of variables in Equation (3), we obtain the following Sturm–Liouville Eigenvalue Problem [57]

$$\begin{cases} \frac{d^2\varsigma_i}{dx^2} + \frac{\omega^2}{gd_i}\varsigma_i = 0; i = 1\ldots N+1; \\ \left.\frac{d\varsigma_1}{dx}\right|_{x=0} = 0;\ \varsigma_i|_{x=L_i} = \varsigma_{i+1}|_{x=L_i};\ \left.\frac{d\varsigma_{N+1}}{dx}\right|_{x=L} = 0; \end{cases} \tag{4}$$

where i is the number of the corresponding section in the channel (Figure 6). These sections differ in the depth of the water channel, so the lower (d_1) and the higher (d_2) values of the depth successively alternate in the channel (Figure 6).

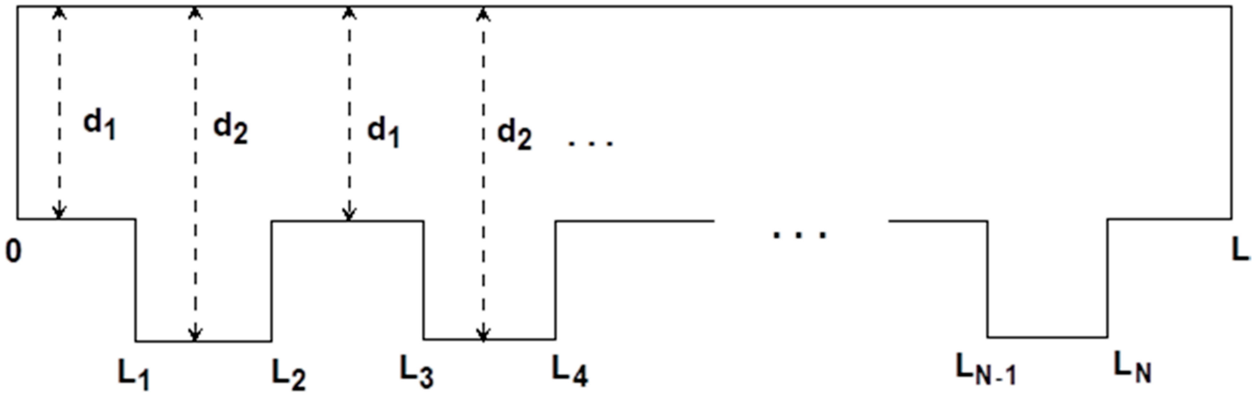

Figure 6. The water channel geometry with the crevasse-ridden bottom, which is considered in the Sturm–Liouville Eigenvalue Problem (4). The channel length $L = 16$ km. The water-layer depth $h_1 = 100$ m.

The eigenmodes and the eigenfrequencies in the problem (4) are expressed as [57]

$$\begin{cases} \varsigma_i^{(n)}(x) = A_i^{(n)}\cos k_i^{(n)} x;\ i = 1\ldots N+1; \\ \omega_n = \frac{\pi\sqrt{gd_1}}{L} n;\ n = 1, 2, \ldots; \end{cases} \tag{5}$$

where $A_i^{(n)}$ is the amplitude of the vibrations in the i-th section ($L_{i-1} < x < L_i$) of the channel and $k_i^{(n)}$ is the wave number ($k_i^{(n)} = \frac{\omega_n}{\sqrt{gd_i}}$).

The amplitudes in Equation (5) are expressed as

$$\begin{cases} A_i^{(n)} = A_1 \frac{\cos\left(\pi\frac{L_1}{L}n\right)\cdot\cos\left(\pi\sqrt{\frac{d_1}{d_2}}\frac{L_2}{L}n\right)\cdot\ldots\cdot\cos\left(\pi\sqrt{\frac{d_1}{d_2}}\frac{L_{i-1}}{L}n\right)}{\cos\left(\pi\sqrt{\frac{d_1}{d_2}}\frac{L_2}{L}n\right)\cdot\cos\left(\pi\frac{L_1}{L}n\right)\cdot\ldots\cdot\cos\left(\pi\frac{L_{i-1}}{L}n\right)},\ i = 2k+1,\ k = 1\ldots P; \\ A_i^{(n)} = A_1 \frac{\cos\left(\pi\frac{L_1}{L}n\right)\cdot\cos\left(\pi\sqrt{\frac{d_1}{d_2}}\frac{L_2}{L}n\right)\cdot\ldots\cdot\cos\left(\pi\frac{L_{i-1}}{L}n\right)}{\cos\left(\pi\sqrt{\frac{d_1}{d_2}}\frac{L_2}{L}n\right)\cdot\cos\left(\pi\frac{L_1}{L}n\right)\cdot\ldots\cdot\cos\left(\pi\sqrt{\frac{d_1}{d_2}}\frac{L_{i-1}}{L}n\right)},\ i = 2k,\ k = 1\ldots P; \end{cases} \tag{6}$$

where A_1 is a given amplitude in the first section ($0 < x < L_1$) and $P = N/2$ is the quantity of the crevasses in the bottom (Figure 6).

Figure 7 shows the relationship between the average amplitude of the eigenmodes defined by Equation (6), and the depth of the crevasses. The average amplitude in Figure 7 was defined as

$$\langle A\rangle = \frac{1}{n_0}\sum_{n=1}^{n_0}\frac{1}{L}\sum_{i=1}^{N+1}\left|A_i^{(n)}\right|(L_i - L_{i-1}), \tag{7}$$

i.e., here the term "average" means both the averaging as across the extension of the channel as across the spectrum.

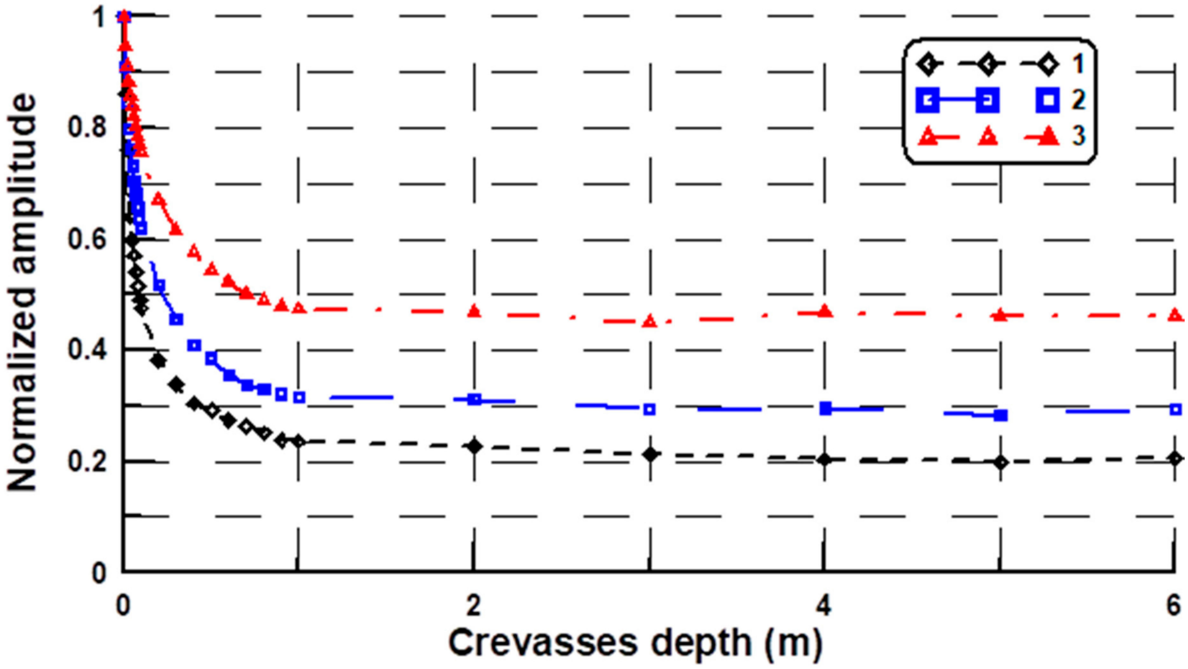

Figure 7. The average normalized amplitude (7) of the gravity waves in the water channel with the crevasse-ridden bottom (Figure 6) versus the depth of the crevasses. Curves 1–3 were, respectively, obtained for the following periodicities of the crevasse locations (1) $\Delta l_{cr} = 1$ km; (2) $\Delta l_{cr} = 2$ km; (3) $\Delta l_{cr} = 4$ km. The width of the crevasses w_{cr} was equal to 0.5 km. The number of eigenmodes n_0 in Equation (7) is equal to 200.

The average amplitude (7) rapidly drops with an increase in the crevasse depth and attains the minimum at $d_{cr} \approx 2$ m (Figure 7). Ultimately, the exact solution (6) reveals relatively high sensitivity with respect to crevasse-depth changes in the range 0–3 m. In opposite to this behavior, the numerical modeling shows that the water layer beneath the ice tongue does not reveal the same sensitivity with regard to the crevasse-depth changes in the range 0–3 m (because the flexural rigidity of the ice tongue is practically unchanged for this range of the crevasse depth variations and for ice thickness equal to 100 m). In particular, the "band gaps" do not appear in the spectra when the crevasse depth changes in the range 0–3 m.

Nevertheless, accounting for the fact that band-gap width causes spectral average amplitude to decrease, we can say that the growth of the band-gap width reaches toward its maximum (Figure 4) and will correlate with a reduction of the average amplitude and a corresponding leveling off of the amplitude at its minimum as in the exact solution (6) (Figure 7).

5. Conclusions

1. The dispersion spectra that embody the relationships between the wave number and periodicity (frequency) of the forcing reveal two types of discontinuities. The first type is the ordinary discretely separated sequence of modes in a regular manner. These regularly spaced mode separations coincide with the minima in the amplitude spectrum. The number of the intermode spaces is approximately equal to the number of the resonant peaks in the amplitude spectra. The intermode spaces are observed both for an intact ice tongue free of the crevasses and for the crevasse-ridden ice tongue. These intermode spaces are caused by the transitions from n-th mode to (n + 1)-th mode, when the new maximum/minimum is added to the previous n-th mode.
2. The second type of discontinuity observed in the dispersion spectra consists of ranges of the frequency where no modes occur at all; these ranges are known as "band gaps" (Freed-Brown et al., 2012). They are observed only for the crevasse-ridden ice tongue.

In particular, for period range 5–250 s considered in this study, there are two "band gaps" for the crevasse-ridden ice tongue. The modes of the ice-tongue vibrations change rapidly inside the "band gaps", and these changes cause the "band gaps". The widths of the "band gaps" depend on the depth of crevasses' penetration into the ice. Essentially, the widths increase with crevasse-depth (d_{cr}) growth, and they attain a maximum at $d_{cr} \approx 30$ m in the model (Figure 4).

3. The exact solutions obtained for the shallow water channel with the crevasse-ridden bottom (Figure 6) likewise reveal that the average amplitude drops as the crevasse-depth increases. Moreover, the average amplitude attains a minimum at $d_{cr} \approx 2$ m and then the amplitude becomes unchanged by further changes in crevasse depth (Figure 7). The minimum level of the average amplitude depends on the periodicity of the crevasses. As the density of crevasses increases (the decrease in the crevasses' periodicity Δl_{cr}), the minimum level of average amplitude decreases (Figure 7).
4. The modeling reveals that the increasing band-gap width causes a decrease in the spectral average amplitude of the vibrations in the vicinity of the "band gaps". Moreover, band-gap width attains a maximum (Figure 4). Thus, achievement of a maximum in the band-gap width provides the achievement of the minimum of the spectral average amplitude of the vibrations in the vicinity of the "band gaps". These results correlate with the results derived from the exact solution (6). The exact solution (6) reveals that the average amplitude of the gravity waves in channel with the crevasse-ridden bottom drops and attains a minimum (Figure 7).

Funding: This research received no external funding.

Data Availability Statement: The basic program code for this research and detailed description of the problem set-up are available at the Zenodo [52] (last accessed January 2021).

Acknowledgments: I thank Douglas R. MacAyeal for helpful discussion of this manuscript and for the comments to this manuscript that allowed me to improve this manuscript. I also thank the referees of the Journal of Marine Science and Engineering for the helpful comments to this manuscript that allowed me to improve this manuscript.

Conflicts of Interest: The author declares no conflict of interest.

References

1. Holdsworth, G.; Glynn, J. Iceberg calving from floating glaciers by a vibrating mechanism. *Nature* **1978**, *274*, 464–466. [CrossRef]
2. Goodman, D.J.; Wadhams, P.; Squire, V.A. The Flexural Response of a Tabular Ice Island to Ocean Swell. *Ann. Glaciol.* **1980**, *1*, 23–27. [CrossRef]
3. Wadhams, P. The seasonal ice zone. In *Geophysics of Sea Ice*; Untersteiner, N., Ed.; Plenum Press: London, UK, 1986; pp. 825–991.
4. Squire, V.A.; Dugan, J.P.; Wadhams, P.; Rottier, P.J.; Liu, A.K. Of ocean waves and sea ice. *Annu. Rev. Fluid Mech.* **1995**, *27*, 115–168. [CrossRef]
5. Meylan, M.H.; Squire, V.A.; Fox, C. Toward realism in modeling ocean wave behavior in marginal ice zones. *J. Geophys. Res. Space Phys.* **1997**, *102*, 22981–22991. [CrossRef]
6. Bromirski, P.D.; Sergienko, O.; MacAyeal, D.R. Transoceanic infragravity waves impacting Antarctic ice shelves. *Geophys. Res. Lett.* **2010**, *37*, 02502. [CrossRef]
7. Bassis, J.N.; Fricker, H.A.; Coleman, R.; Minster, J.-B. An investigation into the forces that drive ice-shelf rift propagation on the Amery Ice Shelf, East Antarctica. *J. Glaciol.* **2008**, *54*, 17–27. [CrossRef]
8. MacAyeal, D.R.; Okal, E.A.; Aster, R.C.; Bassis, J.N.; Brunt, K.M.; Cathles, L.M.; Drucker, R.; Fricker, H.A.; Kim, Y.-J.; Martin, S.; et al. Transoceanic wave propagation links iceberg calv-ing margins of Antarctica with storms in tropics and Northern Hemisphere. *Geophys. Res. Lett.* **2006**, *33*, L17502. [CrossRef]
9. Massom, R.A.; Scambos, T.A.; Bennetts, L.G.; Reid, P.; Squire, V.A.; Stammerjohn, S.E. Antarctic ice shelf disintegration triggered by sea ice loss and ocean swell. *Nature* **2018**, *558*, 383–389. [CrossRef]
10. Bromirski, P.D.; Stephen, R.A. Response of the Ross Ice Shelf, Antarctica, to ocean gravity-wave forcing. *Ann. Glaciol.* **2012**, *53*, 163–172. [CrossRef]
11. Bromirski, P.D.; Diez, A.; Gerstoft, P.; Stephen, R.A.; Bolmer, T.; Wiens, D.A.; Aster, R.C.; Nyblade, A.A. Ross ice shelf vibrations. *Geophys. Res. Lett.* **2015**, *42*, 7589–7597. [CrossRef]
12. Gerstoft, P.; Bromirski, P.; Chen, Z.; Stephen, R.A.; Aster, R.C.; Wiens, D.A.; Nyblade, A.A. Tsunami excitation of the Ross Ice Shelf, Antarctica. *J. Acoust. Soc. Am.* **2017**, *141*, 3526. [CrossRef]

13. Chen, Z.; Bromirski, P.D.; Gerstoft, P.; Stephen, R.A.; Wiens, D.A.; Aster, R.C.; Nyblade, A.A. Ocean-excited plate waves in the Ross and Pine Island Glacier ice shelves. *J. Glaciol.* **2018**, *64*, 730–744. [CrossRef]
14. Chen, Z.; Bromirski, P.D.; Gerstoft, P.; Stephen, R.A.; Lee, W.S.; Yun, S.; Olinger, S.D.; Aster, R.C.; Wiens, D.A.; Nyblade, A.A. Ross Ice Shelf icequakes associated with ocean gravity wave activity. *Geophys. Res. Lett.* **2019**, *46*, 8893–8902. [CrossRef]
15. Godin, O.A.; Zabotin, N. Resonance vibrations of the Ross Ice Shelf and observations of persistent atmospheric waves. *J. Geophys. Res. Space Phys.* **2016**, *121*, 10157. [CrossRef]
16. Robin, G.d.Q. Norwegian-British-Swedish Antarctic Expedition, 1949–1952. *Polar Rec.* **1953**, *6*, 608–616. [CrossRef]
17. Holdsworth, G. Tidal interaction with ice shelves. *Ann. Geophys.* **1977**, *33*, 133–146.
18. Hughes, T. West Antarctic ice streams. *Rev. Geophys.* **1977**, *15*, 1–46. [CrossRef]
19. Lingle, C.S.; Hughes, T.J.; Kollmeyer, R.C. Tidal flexure of Jakobshavns Glacier, west Greenland. *J. Geophys. Res. Space Phys.* **1981**, *86*, 3960. [CrossRef]
20. Stephenson, S.N. Glacier flexure and the position of grounding lines: Measurements by tiltmeter on Rutford Ice Stream, Antarctica. *Ann. Glaciol.* **1984**, *5*, 165–169. [CrossRef]
21. Smith, A.M. The use of tiltmeters to study the dynamics of Antarctic ice shelf grounding lines. *J. Glaciol.* **1991**, *37*, 51–58. [CrossRef]
22. Vaughan, D.G. Tidal flexure at ice shelf margins. *J. Geophys. Res.* **1955**, *100*, 6213–6224. [CrossRef]
23. Schmeltz, M.; Rignot, E.; MacAyeal, D.R. Tidal flexure along ice-sheet margins: Comparison of InSAR with an elastic-plate model. *Ann. Glaciol.* **2002**, *34*, 202–208. [CrossRef]
24. Turcotte, D.L.; Schubert, G. *Geodynamics*, 3rd ed.; Cambridge University Press: Cambridge, UK, 2002.
25. Sergienko, O. Normal modes of a coupled ice-shelf/sub-ice-shelf cavity system. *J. Glaciol.* **2013**, *59*, 76–80. [CrossRef]
26. Sergienko, O.V. Behavior of flexural gravity waves on ice shelves: Application to the Ross Ice Shelf. *J. Geophys. Res. Oceans* **2017**, *122*, 6147–6164. [CrossRef]
27. Papathanasiou, T.K.; Karperaki, A.E.; Theotokoglou, E.E.; Belibassakis, K.A. Hydroelastic analysis of ice shelves under long wave excitation. *Nat. Hazards Earth Syst. Sci.* **2015**, *15*, 1851–1857. [CrossRef]
28. Papathanasiou, T.K.; Karperaki, A.E.; Belibassakis, K.A. On the resonant hydroelastic behaviour of ice shelves. *Ocean Model.* **2019**, *133*, 11–26. [CrossRef]
29. Meylan, M.H.; Bennetts, L.G.; Hosking, R.J.; Catt, E. On the calculation of normal modes of a coupled ice-shelf/sub-ice-shelf cavity system. *J. Glaciol.* **2017**, *63*, 751–754. [CrossRef]
30. Ilyas, M.; Meylan, M.H.; Lamichhane, B.P.; Bennetts, L.G. Time-domain and modal response of ice shelves to wave forcing using the finite element method. *J. Fluids Struct.* **2018**, *80*, 113–131. [CrossRef]
31. Kalyanaraman, B.; Bennetts, L.G.; Lamichhane, B.; Meylan, M.H. On the shallow-water limit for modelling ocean-wave induced ice-shelf vibrations. *Wave Motion* **2019**, *90*, 1–16. [CrossRef]
32. Kalyanaraman, B.; Meylan, M.H.; Bennetts, L.G.; Lamichhane, B.P. A coupled fluid-elasticity model for the wave forcing of an ice-shelf. *J. Fluids Struct.* **2020**, *97*, 103074. [CrossRef]
33. Reeh, N.; Christensen, E.L.; Mayer, C.; Olesen, O.B. Tidal bending of glaciers: A linear viscoelastic approach. *Ann. Glaciol.* **2003**, *37*, 83–89. [CrossRef]
34. Walker, R.T.; Parizek, B.R.; Alley, R.B.; Anandakrishnan, S.; Riverman, K.L.; Christianson, K. Ice-shelf tidal flexure and subglacial pressure variations. *Earth Planet. Sci. Lett.* **2013**, *361*, 422–428. [CrossRef]
35. MacAyeal, D.R.; Sergienko, O.V.; Banwell, A.F. A model of viscoelastic ice-shelf flexure. *J. Glaciol.* **2015**, *61*, 635–645. [CrossRef]
36. Rosier, S.H.R.; Gudmundsson, G.H.; Green, J.A.M. Insights into ice stream dynamics through modeling their response to tidal forcing. *Cryosphere* **2014**, *8*, 1763–1775. [CrossRef]
37. Freed-Brown, J.; Amundson, J.M.; MacAyeal, D.R.; Zhang, W.W. Blocking a wave: Frequency band gaps in ice shelves with periodic crevasses. *Ann. Glaciol.* **2012**, *53*, 85–89. [CrossRef]
38. Van der Veen, C.J. Fracture mechanics approach to penetration of bottom crevasses on glaciers. *Cold Reg. Sci. Technol.* **1998**, *27*, 213–223. [CrossRef]
39. Van der Veen, C.J. Calving glaciers. *Progr. Phys. Geogr.* **2002**, *26*, 96–122. [CrossRef]
40. Scambos, T.A.; Hulbe, C.; Fahnestock, M.; Bohlander, J. The link between climate warming and break-up of ice shelves in the Atlantic Peninsula. *J. Glaciol.* **2000**, *46*, 516–530. [CrossRef]
41. Sheng, P.; Van Tiggelen, B. Introduction to Wave Scattering, Localization and Mesoscopic Phenomena. Second edition. *Waves Random Complex Media* **2007**, *17*, 235–237. [CrossRef]
42. Ashcroft, N.W.; Mermin, N.D. *Solid State Physics*; Books Cole: Belmont, CA, USA, 1976.
43. Mei, C.C. Resonant reflection of surface water waves by periodic sandbars. *J. Fluid Mech.* **1985**, *152*, 315–335. [CrossRef]
44. Chou, T. Band structure of surface flexural–gravity waves along periodic interfaces. *J. Fluid Mech.* **1998**, *369*, 333–350. [CrossRef]
45. Bennetts, L.G.; Biggs, N.R.T.; Porter, D. The interaction of flexural-gravity waves with periodic geometries. *Wave Motion* **2009**, *46*, 57–73. [CrossRef]
46. Bennets, L.; Squire, V. Wave scattering by multiple rows of circular ice floes. *J. Fluid Mech.* **2009**, *639*, 213–238. [CrossRef]
47. Bennets, L.; Williams, T. Wave scattering by ice floes and polynyas of arbitrary shape. *J. Fluid Mech.* **2010**, *662*, 5–35. [CrossRef]
48. Bennetts, L.G.; Squire, V.A. On the calculation of an attenuation coefficient for transects of ice-covered ocean. *Proc. R. Soc. A* **2012**, *468*, 136–162. [CrossRef]

49. Landau, L.D.; Lifshitz, E.M. *Theory of Elasticity*, 3rd ed.; Butterworth-Heinemann: Oxford, UK, 1986; Volume 7.
50. Lurie, A.I. *Theory of Elasticity*; Foundations of Engineering Mechanics; Springer: Berlin/Heidelberg, Germany, 2005.
51. Konovalov, Y.V. Ice-shelf vibrations modeled by a full 3-D elastic model. *Ann. Glaciol.* **2019**, *60*, 68–74. [CrossRef]
52. Konovalov, Y.V. Ice-Shelf Vibrations Modeled by a Full 3-D Elastic Model (Program Code). Zenodo. 2020. Available online: https://doi.org/10.5281/zenodo.4004338 (accessed on 3 January 2021).
53. Schulson, E.M. The Structure and Mechanical Behavior of Ice. *JOM* **1999**, *51*, 21–27. [CrossRef]
54. Shearman, E.D.R. Radio science and oceanography. *Radio Sci.* **1983**, *18*, 299–320. [CrossRef]
55. Landau, L.D.; Lifshitz, E.M. *Fluid Mechanics*; Pergamon Press: New York, NY, USA, 1987; Volume 6.
56. Lamb, H. *Hydrodynamics*, 6th ed.; Cambridge University Press: Cambridge, UK, 1994.
57. Lekner, J. *Theory of Reflection of Electromagnetic and Particle Waves*; Springer: Berlin/Heidelberg, Germany, 1987.